ADVANCED FUNCTIONAL MATERIALS

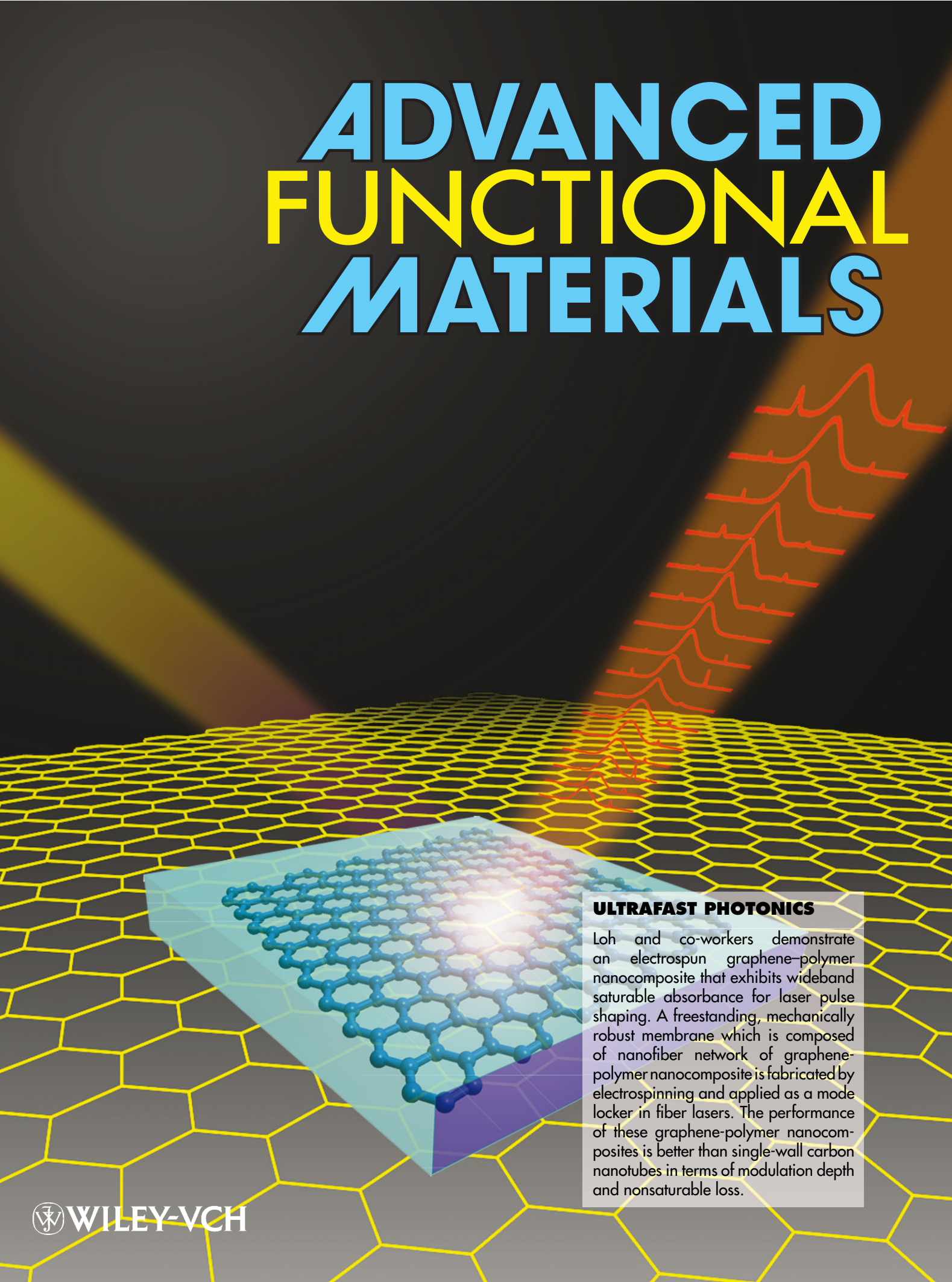

ULTRAFAST PHOTONICS

Loh and co-workers demonstrate an electrospun graphene–polymer nanocomposite that exhibits wideband saturable absorbance for laser pulse shaping. A freestanding, mechanically robust membrane which is composed of nanofiber network of graphene-polymer nanocomposite is fabricated by electrospinning and applied as a mode locker in fiber lasers. The performance of these graphene-polymer nanocomposites is better than single-wall carbon nanotubes in terms of modulation depth and nonsaturable loss.

WILEY-VCH

ADVANCED FUNCTIONAL MATERIALS
www.afm-journal.de

www.MaterialsViews.com

Graphene–Polymer Nanofiber Membrane for Ultrafast Photonics

By *Qiaoliang Bao, Han Zhang, Jia-xiang Yang, Shuai Wang, Ding Yuan Tang, Rajan Jose, Seeram Ramakrishna, Chwee Teck Lim,* and *Kian Ping Loh**

A freestanding membrane composed of a nanofiber network of a graphene–polymer nanocomposite is fabricated by electrospinning and applied as an optical element in fiber lasers. The functionalization of graphene with conjugated organic molecules provides a handle for improving mechanical and thermal properties as well as tuning the optical properties. A small loading (0.07 wt%) of functionalized graphene enhances the total optical absorption of poly(vinyl acetate) (PVAc) by 10 times. The electrospun graphene–polymer nanocomposites exhibit wideband saturable absorbance for laser pulse shaping, and attain a larger modulation depth and smaller nonsaturable loss than single-walled carbon nanotubes. The results show that electrospun graphene nanocomposites are promising candidates as practical and efficient photonic materials for the generation of ultrashort pulses in fiber lasers.

1. Introduction

Polymer nanocomposites combine two concepts in material design, i.e., composites and nanometer-sized materials. Tailor-made nanocomposites which exploit the superlative properties of both components can show enhanced performance in a wide range of applications, from flexible packaging, printable electronics, and interlayer dielectrics to thermoplastics. Polymer nanocomposites that are reinforced with nanofillers such as 1D nanowires[1,2] or 2D layered materials[3–5] exhibit enhanced mechanical, electrical, and thermal properties. Graphite nanoplatelets,[6–8] carbon nanotubes (CNTs),[9–14] graphite oxide,[15–17] and functionalized graphene[18–21] have been used as nanofillers due to their intrinsic mechanical strength. In particular, graphene, a single layer of aromatic carbon, has one of the strongest in-plane bonds among all materials, as well as superior thermal and electrical conductivity. The conjugated graphene sheet can be readily functionalized via noncovalent π–π stacking or covalent C–C coupling reactions. By derivatizing graphene with different organic moieties, the solubility of graphene can be tuned to suit different solvents needed for the processing of composite films. Certain functional groups can broaden the properties of the graphene through the formation of donor–acceptor complexes with graphene, which affords the tunability of electrical conductivity, optical, and photovoltaic properties. It can be expected that based on the superlative properties of graphene and its derivatives, significant improvements in the viscosity and electrical, mechanical, and thermal properties of the graphene–polymer composite can be achieved. For example, it has recently been demonstrated that the properties of functionalized graphene–polymer (i.e., polystyrene and poly(methyl methacrylate) (PMMA)) rival that of single-walled carbon nanotube (SWNT)–polymer composites.[18,19] Graphene should provide good integration with the polymer matrix due to its sheetlike properties, which provide maximal surface area for π–π stacking with polymer hosts. The carboxylic and hydroxyl functional groups on the edges of graphene oxide can also act as linkers for joining organic segments together and impart mechanical strength.

The incorporation of graphene into a polymer matrix can produce a new type of optical material by combining the special optical properties of graphene with the structural properties of the polymer. A single atomic sheet of graphene can absorb $\pi\alpha = 2.3\%$ of incident white light, where α is the fine structure constant.[22] The universal wideband absorption of graphene renders the material attractive as a saturable absorber.[23–25] Its nonlinear optical behavior makes it potentially useful in ultrafast photonics.[26] The use of graphene is inspired by the fact that SWNTs have been used as effective saturable absorbers for the mode-locking of lasers to generate ultrashort pulses in the telecommunication bandwidth.[27,28] SWNTs dispersed in a polymer matrix have proven to be highly effective saturable absorbers due to its ultrafast recovery time and large modulation depth.[29–32] There are no studies thus far on the performance of graphene–polymer

[*] Prof. K. P. Loh, Dr. Q. Bao, Dr. J. Yang, Dr. S. Wang
Department of Chemistry
National University of Singapore
3 Science Drive 3, Singapore 117543 (Singapore)
E-mail: chmlohkp@nus.edu.sg
H. Zhang, Prof. D. Y. Tang
School of Electrical and Electronic Engineering
Nanyang Technological University
Singapore 639798 (Singapore)
Dr. R. Jose, Prof. S. Ramakrishna
Nanoscience and Nanotechnology Initiative
National University of Singapore
Singapore 117576 (Singapore)
Prof. C. T. Lim
Department of Mechanical Engineering & Division of Bioengineering
National University of Singapore
9 Engineering Drive 1, Singapore 117576 (Singapore)

DOI: 10.1002/adfm.200901658

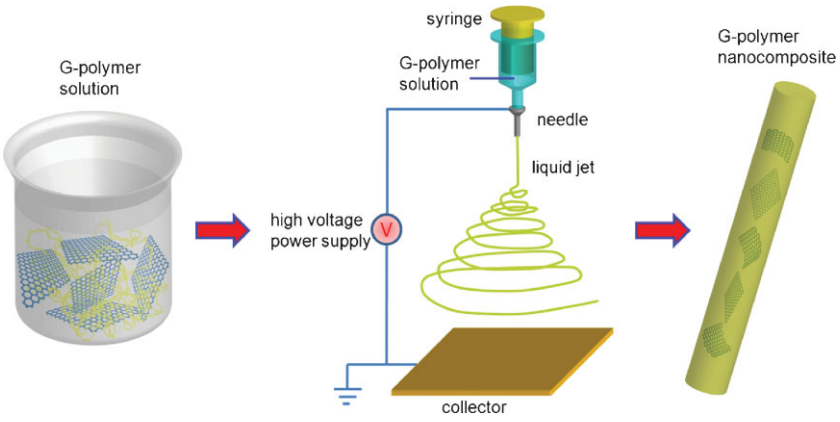

Figure 1. Schematic illustration of the fabrication of graphene–polymer nanofiber composite by electrospinning. G refers to graphene.

composites as saturable adsorbers, so we are motivated to develop a graphene–polymer film that can be used for this purpose.

Electrospinning provides a simple and versatile technique for producing networked membranes from a variety of materials. Such network polymer membranes allow many engineering applications to be enabled, e.g., mechanical reinforcement, water filtration, textile, tissue engineering, and drug release.[33–36] Electrospun polymer fibers can be ultrafine with diameters ranging from nanometers to sub-micrometers, and they can possess high surface-area-to-volume or -mass ratios. Here, we describe an electrospinning process which can incorporate graphene sheets into a continuous nanoscale composite fiber, as illustrated schematically in Figure 1. A freestanding membrane which is composed of a graphene–polymer nanofiber network could be fabricated and applied as an optical element in fiber lasers. Encapsulating graphene in the polymer host passivates the graphene from ambient oxygen, which prevents photo-oxidation and optical bleaching by high-powered lasers. This is very important for developing organic photonics components that do not photodegrade with time. Furthermore, the small diameter of the polymer nanofiber greatly reduces the scattering loss. The functionalization of the graphene, via covalent linking of a dye to the basal plane, as well as noncovalent attachment of aromatic molecules, provides a handle for tuning the optical properties. In this work, we report that electrospun graphene–polymer nanocomposite can be used as an excellent wideband saturable absorber for laser pulse shaping, attaining a larger modulation depth and smaller nonsaturable loss than SWNTs.

2. Results and Discussion

2.1. Graphene Derivatives

The graphene (G) sheets we used were produced by the chemical exfoliation of graphite in acid, which generated soluble precursors such as graphene oxide (GO). The basal planes and edges of GO are decorated with hydroxyl, epoxide, and carboxylic groups; these functional groups provide the tethering sites for the linking of organic molecules. GO can be chemically reduced to G with partial recovery of the π-conjugation, but G has poor solubility in most solvents, and it has to be functionalized further in order to improve its solubility, for example by π–π stacking with hydrophilic aromatic molecules or by coupling to diazonium salts. The main objectives of chemically functionalizing GO or G are to enhance the solubility, improve its dispersion in a polymer matrix, and enrich the optical properties.

We applied four types of graphene derivatives as nanofillers, namely: i) GO, ii) GO noncovalently bonded with poly[(*m*-phenylenevinylene)-*co*-(2,5-dioctoxy-*p*-phenylenevinylene)] (GO-PPV), iii) G modified by 1-pyrenebutanoic acid, succinimidyl ester (G-PBASE), and iv) G functionalized with 4-(2-(pyridin-4-yl)vinlyl) phenyl group (G-dye). Figure 2a shows the chemical structure of these graphene derivatives. Details of the synthesis are provided in the Experimental Section. PPV has been widely investigated because of its nonlinear optical response and electroluminescent activity.[37,38] The functionalization of GO with PPV is expected to impart nonlinear optical properties on the composite. The PPV backbone can undergo π–π stacking on aromatic structures and enhance interfacial bonding in polymeric composites.[39,40] Similarly, PBASE has been used extensively for the noncovalent functionalization and solubilization of carbon nanotubes due to its hydrophilic character.[41] The attachmemt of PBASE via π–π stacking imparts hydrophilic character on the otherwise hydrophobic graphene without disrupting its conjugated network. In the case of G-dye, the dye which is covalently coupled to G has a donor–π-acceptor structure. It is a highly π-conjugated chromophore containing a pyridine moiety (acceptor). The pyridine salt helps to improve the solubility of the systems by introducing an electron-withdrawing group which stabilizes the electron-rich phenylethyl core, and prevents aggregation. This would further broaden the scope of applications, such as graphene-based organic and polymer composite materials.

GO nanosheets can be readily dispersed in water, but show limited solubility in aprotic polar solvents such as *N*,*N*-dimethylformamide (DMF). G-PBASE and G-dye show good polydispersibility, i.e., they can be dispersed in DMF and ethanol and form stable and homogeneous dispersions after ultrasonic treatment (see Fig. 2b). The dispersion of G-dye remains stable for several days compared to GO. Both covalent functionalization, as in the case of GO-dye, as well as noncovalent π–π stacking, as in the case of GO-PPV and G-PBASE, were employed. Figure 3 shows the UV–vis absorption spectra of these graphene derivatives. The maximum absorption of GO occurs at 265 nm, arising from $\pi \rightarrow \pi^*$ transitions of aromatic C=C bonds.[42,43] Graphene sheets that are generated from the chemical reduction of GO possess a higher degree of conjugation due to the removal of the oxygen groups that disrupt the delocalized network; this contributes to a hypochromic shift of the maximum optical absorbance to 275 nm for G-dye. In the case of G-dye, its absorption intensity and range is greatly enhanced and broadened due to the intramolecular charge-transfer and modification of its bandgap. For GO-PPV and G-PBASE, the UV absorption of GO (or G) and the sharp molecular

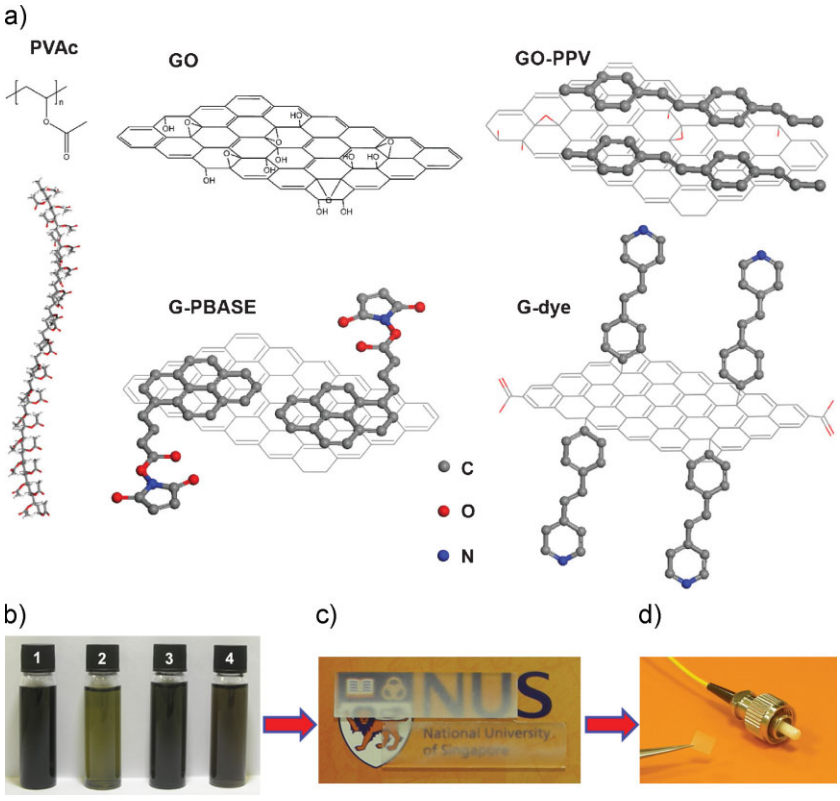

Figure 2. a) Chemical structure of PVAc and graphene-based nanofillers (GO, GO-PPV, G-PBASE, G-dye). b) The dispersions of graphene derivatives 5 h after ultrasonication (1: GO, 2: GO-PPV, 3: G-PBASE, 4: G-dye; all in DMF, 0.15 mg mL^{-1}). c) Typical picture of membranes electrospun on quartz substrates (loading of G-dye: top, 0.07 wt%; bottom, 0.035 wt%). d) Transferring the freestanding membrane onto the end face of an optical fiber for mode-locking.

absorption peaks of organic molecules are overlapped, which is indicative of the presence of two components in the hybrid system, as shown in Figure 3b–c. There is a red-shift of the peak maxima of G-PBASE compared to the free molecular PBASE by 3 nm for the main absorption peaks at 325 and 344 nm (Fig. 3c). This is mainly due to the π–π interactions between the graphene sheets and the aromatic ring of PBASE.[44]

Fourier transform infrared (FTIR) spectroscopy was carried out on the synthesized organic–graphene composites to verify the presence of fingerprint functional groups that should be present from the successful coupling of the organics on G or GO, as shown in Figure 4. The GO spectrum reveals vibration bands corresponding to C=O stretching at 1726 cm^{-1}, C−OH stretching at 1244 cm^{-1}, and C−O stretching at 1053 cm^{-1}.[45,46] The resonance at 1621 cm^{-1} could be due to the vibrations of the adsorbed water molecules or the skeletal vibrations of nonoxidized graphitic domains.[46] In the spectrum of GO-PPV, the sharp adsorption band at 1591 cm^{-1} corresponds to the C=C stretching vibrations, and the peak at 961 cm^{-1} is attributed to the out-of-plane (C−H) bending of trans-substituted vinyl groups.[47,48] These vibrational bands are clear evidences of successful attachment of PPV on GO. In the spectrum of G-PBASE, the peaks at 798 and 1662 cm^{-1} correspond to the out-of-plane vibration of the C−H bond and the C=C stretching vibration of the pyrene ring, respectively. The wide peak centered at 1115 cm^{-1} is due to the stretching vibration of C−C(=O)−O bond of ester.[49,50] The presence of common fingerprint peaks in the FTIR spectra of G-PBASE and pure PBASE suggests successful absorption of PBASE on the graphene skeleton through noncovalent π–π stacking. In comparison with G-PBASE, the FTIR spectrum of G-dye was dominated by a much stronger skeletal band centered at 1601 cm^{-1}, which involves coupled stretching modes in the benzene/pyridine rings (benzene rings from both graphene and dye). The presence of the dye molecules possessing both benzene and pyridine rings are responsible for the greatly enhanced IR absorption intensity.

2.2. Electrospinning

In electrospinning, polymer liquids in solution or molten form are forced under a high DC voltage to become ultrafine fibers with diameters ranging from a few micrometers down to several nanometers. The solvent used to prepare the polymer solution has a predominant influence on its spinnability. For the photonic applications of electrospun graphene–polymer nanocomposites, there are two important considerations for reducing optical losses caused by scattering. First, the refractive index of the polymer host should match that of optical components. Second, the occurrence of "beads" in the fibers should be avoided and the diameters of the nanofibers should be smaller than the optical wavelength. We chose poly(vinyl acetate) (PVAc) as the polymer matrix because its refractive index (n) of 1.47 is close to that of the optics components ($n = 1.45$ for silica).

It is well known that parameters of the polymer solution, such as molecular weight, solution viscosity, surface tension, solution conductivity and dielectric constant, are critical factors that affect the electrospun fiber morphology.[34,35,51] Generally, the formation of "beads" in the fiber is due to the instability of a liquid jet.[51] The solution properties (i.e., viscosity, surface chemistry, and electrical properties) of PVAc are changed remarkably by adding a small amount (0.07 wt%) of graphene derivatives (SWNT was used as a reference). Uniform and smooth nanofibers were readily obtained when G-PBASE and G-dye were used as nanofillers, as shown in Figure 5a–b, while some micrometer-sized beads were formed when GO-PPV was used. In the case of GO and SWNT as nanofillers, numerous beads were obtained (see Fig. S1 in the Supporting Information). Figure 5c–d show representative transmission electron microscopy (TEM) images of G-PBASE/PVAc nanofibers with diameters in the range of 300∼500 nm. The high-magnification TEM image in Figure 5d shows that an individual graphene sheet is well dispersed in the polymer nanofiber matrix. Compared with electrospinning graphite nanoplatelets in the polymer matrix,[52] the good affinity between PVAc and functionalized graphene (G-PBASE and G-dye) result in

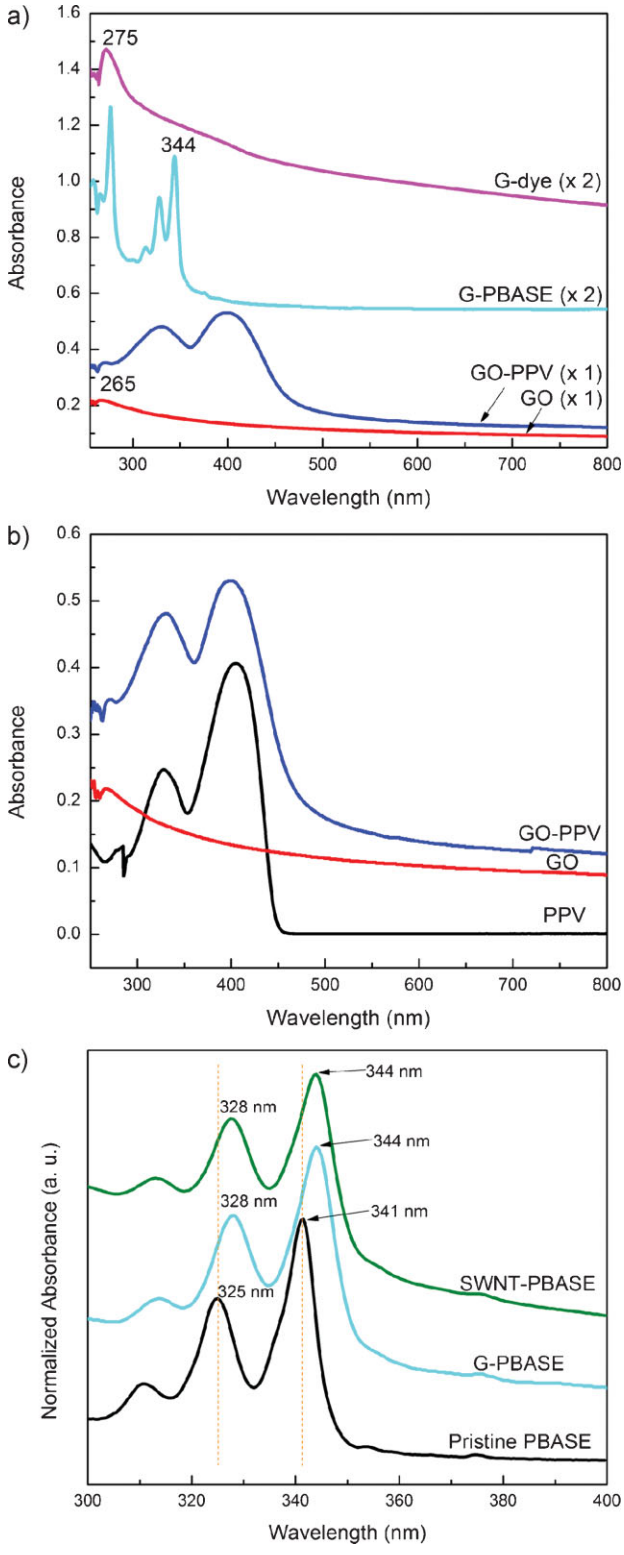

Figure 3. a) UV–vis absorption spectra of graphene derivatives. All the spectra were recorded in DMF with the same concentration (0.05 mg mL^{-1}). b) UV–vis absorption spectra of GO, PPV, and GO-PPV. c) Normalized UV–vis absorption spectra of pristine PBASE, G-PBASE and SWNT-PBASE. The spectra of G-PBASE and SWNT-PBASE have been offset for better view.

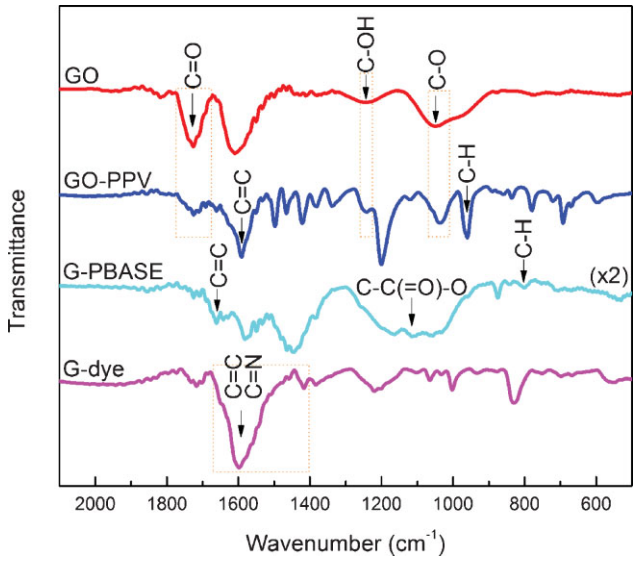

Figure 4. FTIR spectra of the various graphene derivatives.

uniform fibers with no beading. In contrast, the formation of beads when plain GO (shown in Fig. S1e, Supporting Information) is used as the nanofiller is due to the poor dispersion[18] of GO in DMF, the solvent used in electrospinning. The bundling and aggregation of SWNTs also result in the formation of numerous large beads,[53] as shown in Figure S1f (Supporting Information).

2.3. Mechanical Properties

The mechanical properties of the electrospun nanocomposite membranes were investigated by the tensile stress–strain testing method.[54] Mechanical reinforcement can be achieved when the nanofiller is dispersed homogeneously in the matrix and the external load is efficiently transferred via strong interaction at the interface between the filler and matrix. In order to investigate how the intrinsic properties of the graphene derivatives affect the properties of polymer host, parameters such as the concentration of PVAc, the weight fraction of nanofillers, and the electrospinning process parameters were standardized for all the test samples. The representative stress–strain curves of these graphene-based PVAc nanocomposites are shown in Figure 6. Yield points (maximum in the peak) associated with a deformation mechanism can be observed for the different composites. From the steeper slope of the stress–strain curve for the composites compared to PVAc, it is clear that G-PBASE, G-dye, and SWNTs can enhance the Young's modulus (slope of the stress–strain curve) of PVAc. The averaged tensile modulus and the ultimate tensile strength of the respective graphene nanocomposites are summarized in Table 1 (also see Fig. S2 (Supporting Information) for the full-range stress–strain curves). All the nanofillers enhance the strength of PVAc to various extent. For example, with only 0.07 wt% of G-PBASE, the ultimate strength increases by 102% from 6.13 to 12.39 MPa, which is the highest among the graphene nanofillers used here. GO/PVAc has the lowest ultimate strength of 8.5 MPa among these nanocomposites, which is also 1.39 times larger than pure PVAc. From the

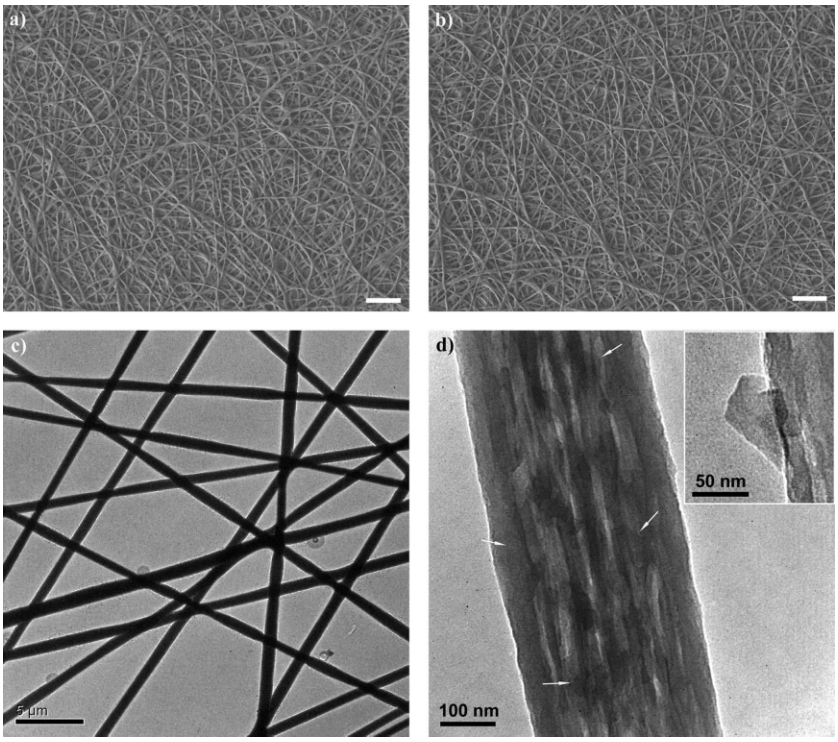

Figure 5. a–b) Scanning electron microscopy (SEM) images of the graphene–polymer nanocomposite membrane fabricated by electrospinning: G-PBASE/PVAc (a) and G-dye/PVAc (b); scale bars: 10 μm. c) TEM image of G-PBASE/PVAc nanofibers. d) High-magnification TEM image of G-PBASE/PVAc nanofiber. The arrows indicate the graphene flakes inside the nanofiber. The inset shows an enlarged image of G-PBASE embedded in the sidewall of a PVAc nanofiber.

results shown in Figure 6 and Table 1, it is clear that G-PBASE/PVAc and G-dye/PVAc exhibit superior performance. One reason is the good molecular-level dispersion of G-PBASE and G-dye in DMF and the PVAc matrix. The oxygen atoms in G-PBASE and the pyridinium nitrogen in G-dye afford hydrogen bonding interactions with the PVAc chains (Fig. S3, Supporting Information). These intermolecular hydrogen bonding interactions will increase the viscosity of the polymer host.[55,56] When the matrix is subjected to loading, the strain is transferred to graphene, which has one of the highest in-plane bonds of all materials. The improved dispersion of the functionalized graphene in the polymer matrix coupled with an increase in the interfacial bond strength is likely the mechanism for the increased load transfer effectiveness.

2.4. Thermal Properties

The thermal properties of these graphene-based nanocomposites are also improved owing to the presence of interfacial bonding. The thermogravimetric analysis (TGA) and differential thermogravimetric (DTG) curves are shown in Figure 7. For pristine PVAc nanofibers, the first major weight loss occurs at ~330 °C and the second at ~438 °C, which is consistent with the degradation pattern of PVAc.[57] For the electrospun graphene–PVAc nanocomposites, the major weight loss of ~65% (Fig. 7a) occurs in a similar temperature range of 285~375 °C, which corresponds to the thermal decomposition of the polymer backbone.[58] The subsequent weight loss at ~438 °C is attributed to the destruction of the functional moieties (such as carbonyl group, PPV, PBASE, and dye). The weight loss above 500 °C is due to combustion of the carbon skeleton (see Fig. S4a, Supporting Information). Three exothermic peaks at ~334, ~438, and >500 °C are clearly resolved in the DTG curves, as shown in Figure 7b. A higher thermal stability is reflected by the lower peak intensity and higher peak position in the DTG curves. The incorporation of 0.07 wt% graphene derivatives increases the onset decomposition temperature of PVAc by 2 to 5 °C (inset of Fig. 7b). The decomposition temperature of the carbon skeleton is increased by 20~90 °C. The decomposition temperature increases with higher concentration of graphene-based nanofillers (Fig. S4b, Supporting Information).[19,59] A qualitative analysis of the decomposition behavior reveals that the carbon skeletons in G-PBASE/PVAc and G-dye/PVAc exhibit higher decomposition temperature and yield larger amount of residue compared to PVAc.

2.5. Optical Properties

The linear and nonlinear optical absorption of the electrospun membranes were investigated. Figure 8a compares the absorption spectra of graphene-based polymer composite thin films with a thickness of ~10 μm (checked by scanning electron microscopy (SEM)). The absorption spectra of pure PVAc and SWNT/PVAc are also shown for

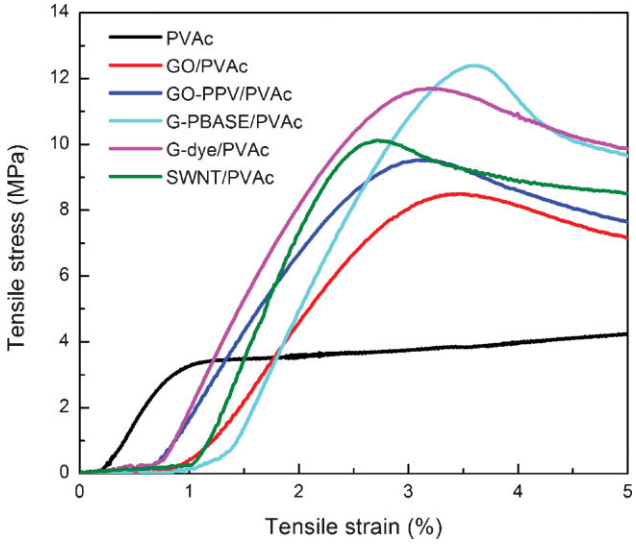

Figure 6. Tensile stress–strain curves of electrospun graphene-based PVAc composites.

Table 1. Tensile properties of the electrospun nanocomposite membranes.

	Young's modulus	Ultimate strength	Yield strength	Breaking strength	Maximal deformation
	[GPa]	[MPa]	[MPa]	[MPa]	[%]
PVAc	0.513	6.13	3.45	6.13	12.4
GO/PVAc	0.465	8.5	8.5	5.77	16.6
GO-PPV/PVAc	0.453	9.52	9.52	7.44	96.8
G-PBASE/PVAc	0.642	12.39	12.39	7.93	52.0
G-dye/PVAc	0.598	11.78	11.70	11.4	82.5
SWNT/PVAc	0.744	10.13	10.13	7.86	9.3

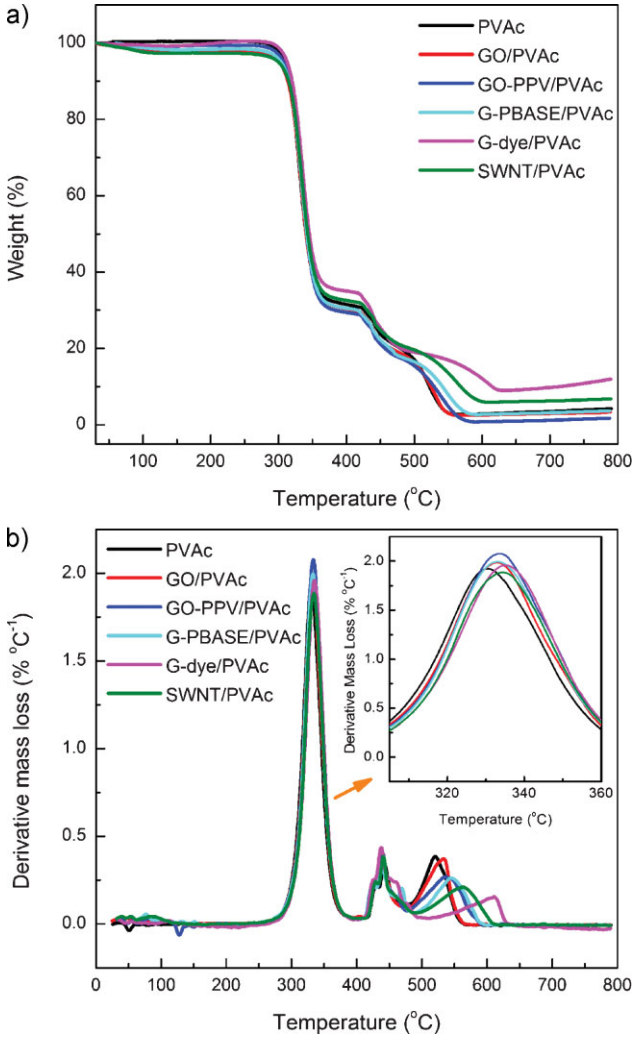

Figure 7. a) TGA and b) DTG analyses of PVAc and four types of graphene-based and SWNT-based polymer nanocomposites. The inset in b shows the enlarged DTG peak at ~330 °C.

comparison. After incorporating the graphene nanofillers into the PVAc host, the absorption increases in the 400–800 nm range compared to the spectra taken in the DMF solution. This is due to the absorption contribution of the polymer host and scattering effects of the nanofibers. Optical scattering by the nanofibers

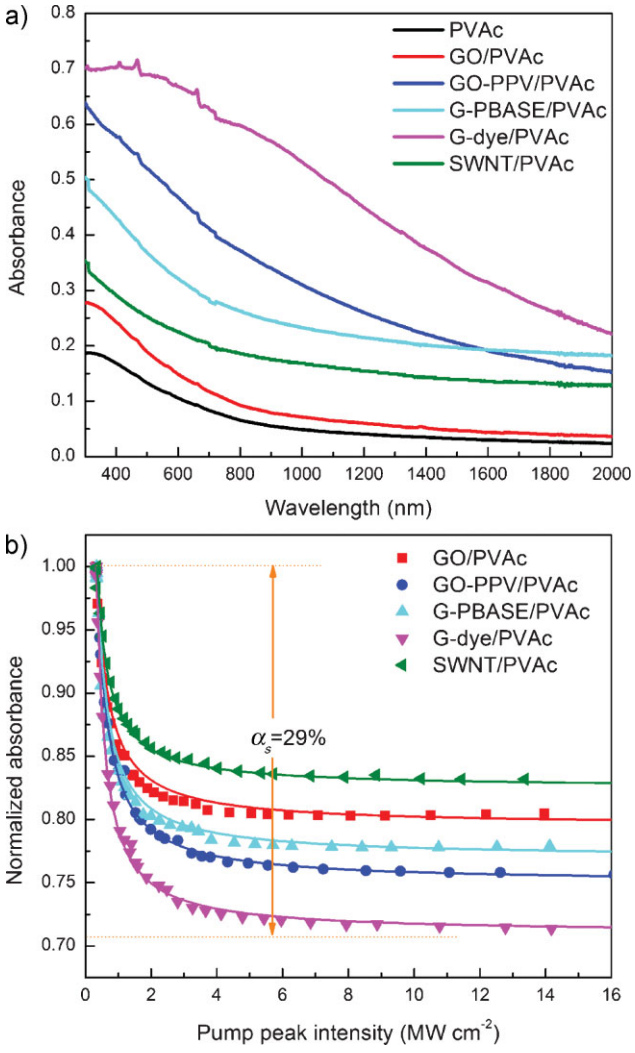

Figure 8. a) UV–vis–NIR absorption spectra of graphene-based PVAc nanocomposites. b) Power-dependent nonlinear saturable absorption of graphene-based PVAc nanocomposites. α_s refers to percent saturable absorption component.

occurs mainly at wavelengths comparable to the nanofiber diameters (300~500 nm); therefore the transmission at the longer-wavelength range will increase. After subtracting the absorbance contribution of PVAc, the absorption by G-PBASE can be estimated to be ~36% of input light at 400 nm, with about ~9% scattering loss by the nanofibers.

Due to the transparency of GO, adding 0.07 wt% GO as nanofiller only slightly enhanced the total absorption. In contrast, adding 0.07 wt% G-dye results in strong wideband absorption from the visible to near infrared (NIR) region because of the strong absorption of G-dye. Charge transfer interaction causes the absorption maxima of the polymer composite to red-shift from that of the G-dye by as much as 200 nm to 470 nm. Pure PVAc is highly transparent in the telecommunication window (around 1550 nm) with a relative low absorbance of 0.03 (equal to a transmission loss of 0.3 dB). Remarkably, the graphene–polymer composites exhibit enhanced absorbance at this region compared with the pure polymer system. For example, at 1550 nm, the absorbance is

1.5 times for GO/PVAc, 6.4 times for GO-PPV/PVAc, 6.2 times for G-PBASE/PVAc, and 10.5 times for G-dye/PVAc (4.4 times for SWNT/PVAc) compared to pure PVAC. The wideband strong IR absorbance makes these composites attractive as saturable absorbers for fiber lasers.

The nonlinear absorption properties of our composites are studied by power-dependent measurements at 1550 nm (See Experimental Section), as shown in Figure 8b. The saturation of absorption could be seen quite clearly with the increase of incident light intensity. The absorption as a function of increasing light intensity can be fitted by[60]

$$\alpha(I) = \frac{\alpha_s}{1 + I/I_S} + \alpha_{NS} \quad (1)$$

where α_s and α_{NS} are the saturable and nonsaturable absorption and I_S is the saturation intensity, defined as the optical intensity required in a steady state to reduce the absorption to half of its unbleached value. This yields a saturation intensity ranging from 0.5 to 0.7 MW cm^{-2}, which is much smaller than that reported for SWNTs[27,31,32] and semiconductor saturable absorber mirrors (SESAMs).[61] Most importantly, the graphene-based polymer composites exhibit a larger modulation depth (saturable absorption component) than the SWNT/PVAc composite, as summarized in Table 2. For example, among the several types of graphene–polymer composites, the G-dye/PVAc composite shows the largest saturable absorption component of 29%, which is two times that of the SWNT/PVAc composite. The large modulation depth and high ratio of saturable-to-nonsaturable absorption indicate stronger noise suppression and pulse shaping ability,[62] making these composites promising as noise suppressors and saturable absorbers.

The large modulation depth of graphene–polymer composites is related to their relatively low nonsaturable loss. Nonsaturable loss generally arises from scattering losses by defects or aggregates, nonsaturable absorption from the polymer host, reflection at the membrane surface and coupling loss in fibers. The selection of PVAc as the polymer host is guided by its matching refractive index with the optical fiber, which reduces reflection at the membrane surface. The low scattering loss of graphene–polymer composites is attributed to the good dispersion of the 2D graphene nanosheets in the polymer nanofibers. The fabrication of composite nanofibers with diameters much smaller than the working wavelength (1550 nm) also helps to reduce scattering loss. In contrast, the micrometer-sized beads occurring in SWNT/PVAc are responsible for inducing large scattering and contribute to significant nonsaturable loss.

Table 2. Optical properties of graphene-based PVAc nanocomposites.

	Absorbance (at 1550 nm)	Saturable absorption	Saturation intensity
		[%]	[MW cm^{-2}]
GO/PVAc	0.046	20.5	0.62
GO-PPV/PVAc	0.198	25	0.68
G-PBASE/PVAc	0.194	23	0.59
G-dye/PVAc	0.326	29	0.60
SWNT/PVAc	0.138	17.5	0.71

2.6. Ultrafast Photonics

The enhanced broadband absorption of the graphene–polymer composites motivated us to investigate its applications in ultrafast photonics. The intensity-dependent attenuation discussed above has important applications in ultrafast photonics because of its pulse shaping; i.e., a saturable adsorber is transparent to the high intensity components of an optical pulse, but opaque to the lower intensity components of the pulse.[63] Therefore, a saturable adsorber suppresses continuous wave (CW) radiation and enhances short pulse generation when it is incorporated into a laser cavity. In this work, our graphene–polymer nanocomposite membranes were attached onto the end faces of optical fibers (Fig. 2d) to function as a passive mode-locker in a ring cavity fiber laser (see Fig. S5 (Supporting Information) for the ring laser cavity configuration).

A series of experiments show that mode-locking can be achieved from all these graphene-based polymer composites above a pump power of ~25 mW. The basic operation of the laser is described in the Experimental Section. For the composites with larger modulation depth, the mode-locking status is more stable and exhibits ease of self-starting above the pump threshold. Here we focus our discussion on the mode-locking performance of G-dye/PVAc since it has the highest modulation depth among the graphene-based polymer composites. The typical pulse train of the laser output, depicted in Figure 9a, verifies the pulse formation with a repetition rate of 6.95 MHz, which matches with the cavity roundtrip time. The autocorrelation (AC) trace of the mode-locked pulses is shown in Figure 9b, which is well fitted by a sech^2 (square of the hyperbolic secant) function with full width at half maximum (FWHM) of 1.67 ps. This gives a pulse width of 1.08 ps by multiplying the FWHM of the AC trace by the decorrelation factor (0.648). The time-bandwidth product of the mode-locked pulses is about 0.4, indicating that the pulses are slightly chirped. The radio-frequency (RF) spectrum of the mode-locked pulses was also measured after optical-to-electrical conversion using a fast photodiode, as shown in Figure 9c. A 58 dB peak-to-background ratio (~10^6 contrast) is observed for the fundamental peak centered at the cavity repetition rate (6.95 MHz).

Most importantly, a tuning range of 30 nm (1570–1600 nm) of the laser output was achieved from G-PBASE/PVAc and G-dye/PVAc, as shown in Figure 9d. All the output spectra as a function of wavelength show two discrete spectral sidebands, indicating the soliton operation of the laser.[61] Soliton refers to any optical field that does not change during propagation because of a delicate balance between nonlinear and linear effects in the medium. It is well known that the soliton pulse in fiber optics generated by the balance between the self-phase modulation (SPM) and the negative group velocity dispersion (GVD) is short and stable.[64] The solitonic sidebands are unambiguous evidence of stable mode-locking of the fiber laser in the tuning range. In addition, the mode-locking can be operated for three days continuously and the output laser pulses maintain high stability, i.e., the fluctuation of peak position is within 0.3 nm and the peak intensity varies within 0.15 dB (Fig. 9e).

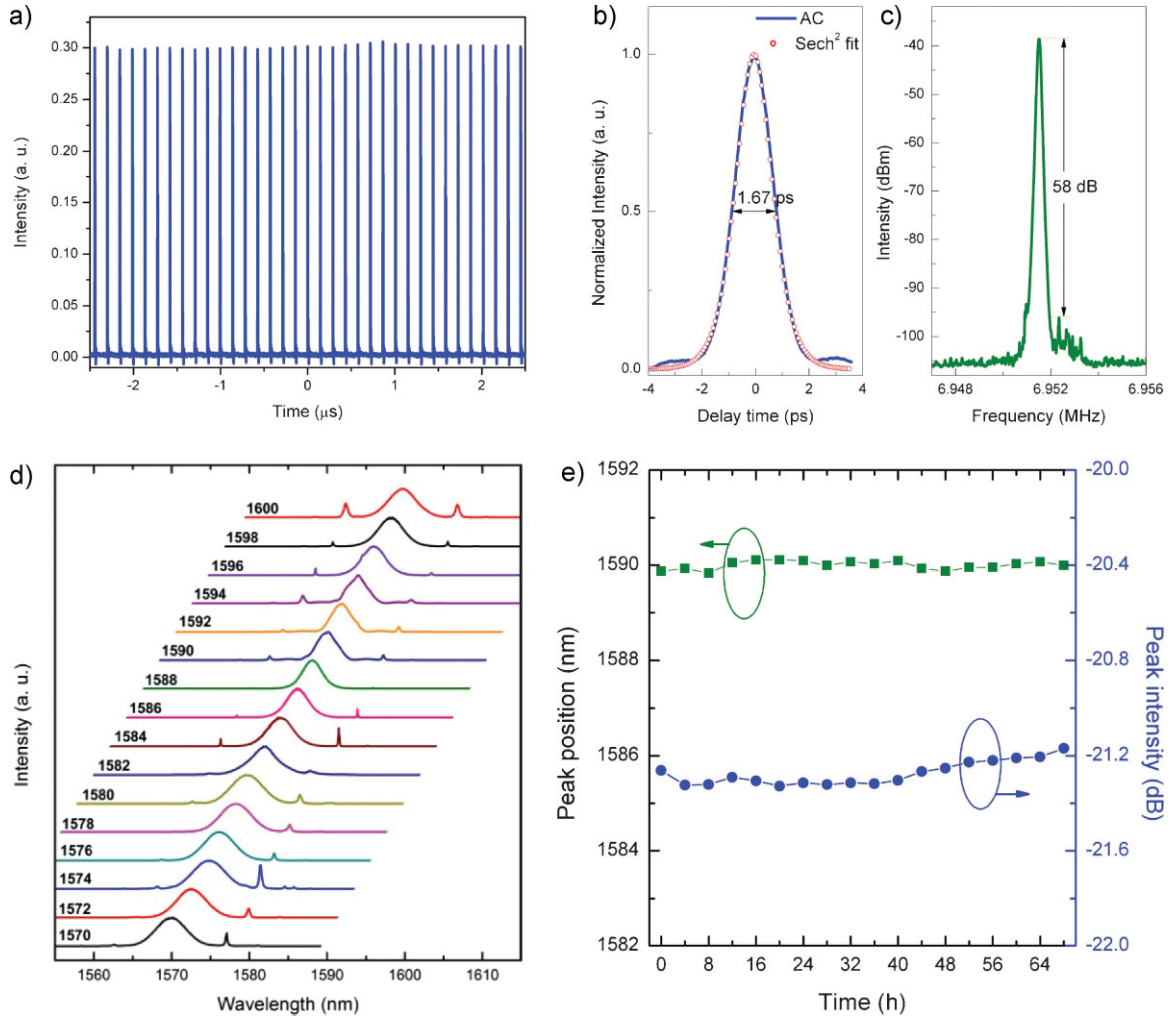

Figure 9. Mode-locking characteristics at 1590 nm. a) Output pulse train. b) AC trace and sech^2 fitting curve. c) Radio frequency spectrum of mode-locking pulses. d) Wideband output spectra from 1570 to 1600 nm. e) The long-term stable operation of mode-locking at 1590 nm. The data were collected every 4 h for 68 h.

At present, there is a lot of interest in using carbon nanotube-based nanocomposites as saturable absorbers. The optical properties of the graphene-based nanocomposites in this work compete favorably with the best performance reported in the literature for SWNT–polymer composites.[31,32] The saturable absorption modulation depth of our composites with 0.07 wt% loadings range from 20% to 29%, which is generally higher than SWNT–polymer composites (4∼17%).[31,32,65,66] The modulation depth can be tuned further by varying the concentration of graphene derivatives in the composite. In principle, the graphene–polymer composites can function better than SWNT as full-waveband saturable absorber due to its strong broadband absorption.

Finally, the mode-locking performance of the graphene–polymer composites was compared with that of the conventional saturable absorber: SESAM. It is found that with graphene–polymer composites as the mode-locker, mode-locking can be easily achieved in a wide wavelength range; i.e., continuous soliton central wavelength tuning as large as 30 nm can be obtained, and the mode-locked pulses have very large single-pulse energy (as large as several nanojoules[24]). With a SESAM as the mode-locker,[67] mode-locking can only be achieved in a much narrower wavelength range (only ∼10 nm), and the mode-locked pulses can only have a much smaller single-pulse energy due to the break up into multiple pulses in cavity.

3. Conclusions

In summary, graphene-based polymer nanocomposites are remarkable materials that combine the chemically tunable optoelectronic properties of graphene derivatives with the mechanical, thermal properties, and processing advantages of plastics. We have demonstrated a quasi-industrial approach based on electrospinning to fabricate graphene–polymer nanocomposites. Chemically functionalized graphene derivatives are

incorporated into polymer matrix to reinforce the mechanical, thermal, and optical properties. Our results show that electrospun nanocomposites are promising candidates as saturable absorber with wideband absorption and can be used as a practical and efficient photonic material for the generation of ultrashort pulses in fiber lasers. Coupled with intelligent laser cavity designing and fiber gain engineering, we believe that full-waveband ultrafast lasers can be realized using graphene–polymer composites.

4. Experimental

Sample Synthesis: *GO*. Graphene oxide was synthesized from graphite using a modified Hummer's method. Briefly, graphite flakes (1.5 g) were slowly added into H_2SO_4 (69 mL) with vigorous stirring in an ice-water bath. After the graphite forms a black slurry, $NaNO_3$ (1.5 g) was slowly added over 15 min. The mixture was then allowed to warm to room temperature and stirred for 1 h. Water (120 mL) was added to the solution followed by stirring for 30 min at 90 °C. The mixture was poured into 300 mL of water, followed by slowly adding H_2O_2 (10 mL). The solution was filtered after the color of the solution changed from dark brown to yellow. The resultant material was redispersed in water and filtered several times until the pH of the filtrate was neutral. Finally, the filtrate was dried in vacuum overnight to obtain the GO product. *GO-PPV*. Dried GO (1 mg) was dispersed in 10 mL of DMF by sonication. Then, PPV (1 mg) was added to the dispersion and heated to 80 °C for 24 h. Ethanol (50 mL) was added to the product for centrifuging to obtain GO-PPV. The resultant GO-PPV was then washed with ethanol and dried in vacuum. *G-PBASE*. GO (1 mg) was dispersed in DMF (10 mL) by sonication. PBASE (1 mg) and hydrazine monohydrate (100 μL) were added to the dispersion and heated to 80 °C for 24 h to facilitate the reduction of GO. The product was centrifuged in ethanol (50 mL), washed, and dried in vacuum. *G-dye*. Synthesis of G-dye involved the complete exfoliation of graphite into individual GO sheets, followed by reduction to produce individual graphene sheets. The graphene sheets were functionalized with the phenyl bromide group using the diazonium coupling reaction, and then reacted with 4-vinylpyridine using the Heck reaction. *SWNT*. SWNTs (1 mg) purchased from Sigma with a purity of 85% were dispersed in DMF (10 mL) by ultrasonication. Afterwards, PBASE (1 mg) was added to the dispersion and heated to 80 °C for 24 h. The product was centrifuged in 50 mL of ethanol to obtain SWNT-PBASE. The resultant SWNT-PBASE was washed with ethanol and dried in vacuum.

Electrospinning: PVAc (number-averaged molecular weight, $M_n = 500\,000$) was obtained from Sigma-Aldrich. The as-synthesized graphene derivative (0.47 mg) was dispersed in DMF (1 mL) by ultrasonication. The solution was mixed with PVAc solution (3 mL, 23.5 wt%) in DMF and then stirred for 24 h at 60 °C in sealed bottles to form the wet paste for electrospinning. The electrospinning was carried out in a MECC NANON ELECTROSPINNING set up. The optimized electrospinning parameters were an applied voltage of 30 kV, feeding rate of 0.5 mL h^{-1}, and needle-tip-to-collector distance of 100 mm. During electrospinning, the needle was scanned above a collector made of aluminum foils for 5 min to form a membrane of 150 mm × 20 mm and a thickness of ~10 μm.

Characterization: The morphologies of G–polymer nanocomposites were investigated by optical microscopy and scanning electron microscopy (SEM, JSM-6700F, JEOL). The microstructures of the graphene–polymer nanocomposites were characterized by TEM (3010, 200 kV, JEOL). The G–polymer nanofibers were directly electrospun on carbon-coated copper grids for TEM investigation. Optical absorption spectra from the UV to NIR region were baseline-corrected against the corresponding solvents on a Shimadzu 3600 spectrophotometer. The functional groups in GO/G were examined using a FTIR spectrometer (Varian 3100). The mechanical properties of PVAc/graphene nanocomposites were measured by a tabletop Instron tester at 24 °C with 40% relative humidity [54]. The extension rate was 5 mm min^{-1} and the load cell was 100 N with a gauge length of 30 mm. All samples were cut into strips of 50 mm × 10 mm. In all cases, three samples were tested from which the mean and standard deviation were calculated. TGA was carried out on TA Instruments (SDT 2960). The heating rate was 10 °C min^{-1}. Approximately 5 mg of each sample was measured in a ceramics crucible in air.

Ultrafast Photonics: A stable and standard soliton mode-locked fiber laser with output pulse width of 1 ps and repetition rate of 100 MHz was used as the input seed pulse for nonlinear absorption measurements, similar to our previous work [23]. For the application of graphene-based polymer nanocomposite in ultrafast photonics, we used the standard fiber-optic components, such as wavelength division multiplexer (WDM), polarization controller, coupler, optical isolator, erbium-doped fiber (EDF), and single-mode fiber (SMF); Fig. S5 in Supporting Information shows the laser cavity configuration. In order to utilize both the highly efficient amplification and wave-breaking-free effect, a piece of EDF (5.0 m, 2880 ppm) with GVD of -32 ps nm^{-1} km^{-1} was adopted as the gain fiber. SMF (23.8 m) with GVD 18 ps nm^{-1} km^{-1} was employed in the cavity to compensate the normal dispersion from EDF and ensure the operation of the cavity in the conventional nonlinear Schrödinger equation soliton regime. Accordingly, the net cavity dispersion is still anomalous at about -0.3419 ps^2. A 30% fiber coupler was used to output the signal, and the laser was pumped by a high-power fiber Raman laser source (KPS-BT2-RFL-1480-60-FA) of wavelength 1480 nm. The maximum pump power can reach as high as 5 W. A polarization independent isolator was spliced in the cavity to force the unidirectional operation of the ring cavity. Intracavity polarization controllers were used to alter the cavity linear birefringence. An optical spectrum analyzer (Ando AQ-6315B) and a 350 MHz oscilloscope (Agilent 54641A) combined with a 2 GHz photodetector were used to simultaneously monitor the spectra and pulse train, respectively.

Acknowledgements

The authors thank the NRF-CRP grant ''Graphene Related Materials and Devices'' R-143-000-360-281. Supporting Information is available online from Wiley InterScience or from the author.

Received: September 3, 2009
Published online: February 9, 2010

[1] C. Y. Chang, F. C. Tsao, C. J. Pan, G. C. Chi, H. T. Wang, J. J. Chen, F. Ren, D. P. Norton, S. J. Pearton, K. H. Chen, L. C. Chen, *Appl. Phys. Lett.* **2006**, *88*, 173503.
[2] S. R. C. Vivekchand, U. Ramamurty, C. N. R. Rao, *Nanotechnology* **2006**, *17*, S344.
[3] S. S. Ray, M. Okamoto, *Prog. Polym. Sci.* **2003**, *28*, 1539.
[4] P. G. Emmanuel, *Adv. Mater.* **1996**, *8*, 29.
[5] N. Sheng, M. C. Boyce, D. M. Parks, G. C. Rutledge, J. I. Abes, R. E. Cohen, *Polymer* **2004**, *45*, 487.
[6] W. Zheng, S. C. Wong, *Compos. Sci. Technol.* **2003**, *63*, 225.
[7] T. Ramanathan, S. Stankovich, D. A. Dikin, H. Liu, H. Shen, S. T. Nguyen, L. C. Brinson, *J. Polym. Sci, Part B: Polym. Phys.* **2007**, *45*, 2097.
[8] K. Wakabayashi, C. Pierre, D. A. Dikin, R. S. Ruoff, T. Ramanathan, L. C. Brinson, J. M. Torkelson, *Macromolecules* **2008**, *41*, 1905.
[9] P. M. Ajayan, L. S. Schadler, C. Giannaris, A. Rubio, *Adv. Mater.* **2000**, *12*, 750.
[10] L. N. An, W. X. Xu, S. Rajagopalan, C. M. Wang, H. Wang, Y. Fan, L. G. Zhang, D. P. Jiang, J. Kapat, L. Chow, B. H. Guo, J. Liang, R. Vaidyanathan, *Adv. Mater.* **2004**, *16*, 2036.
[11] J. N. Coleman, U. Khan, Y. K. Gun'ko, *Adv. Mater.* **2006**, *18*, 689.
[12] J. C. Grunlan, A. R. Mehrabi, M. V. Bannon, J. L. Bahr, *Adv. Mater.* **2004**, *16*, 150.
[13] E. Munoz, D. S. Suh, S. Collins, M. Selvidge, A. B. Dalton, B. G. Kim, J. M. Razal, G. Ussery, A. G. Rinzler, M. T. Martinez, R. H. Baughman, *Adv. Mater.* **2005**, *17*, 1064.

[14] T. Ramanathan, H. Liu, L. C. Brinson, *J. Polym. Sci., Part B: Polym. Phys.* **2005**, *43*, 2269.
[15] N. I. Kovtyukhova, P. J. Ollivier, B. R. Martin, T. E. Mallouk, S. A. Chizhik, E. V. Buzaneva, A. D. Gorchinskiy, *Chem. Mater.* **1999**, *11*, 771.
[16] N. A. Kotov, I. Dekany, J. H. Fendler, *Adv. Mater.* **1996**, *8*, 637.
[17] T. Cassagneau, F. Guerin, J. H. Fendler, *Langmuir* **2000**, *16*, 7318.
[18] S. Stankovich, D. A. Dikin, G. H. B. Dommett, K. M. Kohlhaas, E. J. Zimney, E. A. Stach, R. D. Piner, S. T. Nguyen, R. S. Ruoff, *Nature* **2006**, *442*, 282.
[19] T. Ramanathan, A. A. Abdala, S. Stankovich, D. A. Dikin, M. Herrera-Alonso, R. D. Piner, D. H. Adamson, H. C. Schniepp, X. Chen, R. S. Ruoff, S. T. Nguyen, I. A. Aksay, R. K. Prud'homme, L. C. Brinson, *Nat. Nanotechnol.* **2008**, *3*, 327.
[20] R. Verdejo, F. Barroso-Bujans, M. A. Rodriguez-Perez, J. A. de Saja, M. A. Lopez-Manchado, *J. Mater. Chem.* **2008**, *18*, 2221.
[21] J. L. Vickery, A. J. Patil, S. Mann, *Adv. Mater.* **2009**, *21*, 2180.
[22] R. R. Nair, P. Blake, A. N. Grigorenko, K. S. Novoselov, T. J. Booth, T. Stauber, N. M. R. Peres, A. K. Geim, *Science* **2008**, *320*, 1308.
[23] Q. Bao, H. Zhang, Y. Wang, Z. Ni, Y. Yan, Z. X. Shen, K. P. Loh, D. Y. Tang, *Adv. Funct. Mater.* **2009**, *19*, 3077.
[24] H. Zhang, Q. Bao, D. Y. Tang, Luming Zhao, K. P. Loh, *Appl. Phys. Lett.* **2009**, *95*, 141103.
[25] H. Zhang, D. Y. Tang, L. M. Zhao, Q. Bao, K. P. Loh, *Optics Express* **2009**, *17*, 17630.
[26] J. M. Dawlaty, S. Shivaraman, M. Chandrashekhar, F. Rana, M. G. Spencer, *Appl. Phys. Lett.* **2008**, *92*, 042116.
[27] S. Y. Set, H. Yaguchi, Y. Tanaka, M. Jablonski, *IEEE J. Sel. Top. Quantum Electron.* **2004**, *10*, 137.
[28] S. Yamashita, Y. Inoue, S. Maruyama, Y. Murakami, H. Yaguchi, M. Jablonski, S. Y. Set, *Opt. Lett.* **2004**, *29*, 1581.
[29] A. G. Rozhin, Y. Sakakibara, S. Namiki, M. Tokumoto, H. Kataura, Y. Achiba, *Appl. Phys. Lett.* **2006**, *88*, 051118.
[30] A. V. Tausenev, E. D. Obraztsova, A. S. Lobach, A. I. Chernov, V. I. Konov, P. G. Kryukov, A. V. Konyashchenko, E. M. Dianov, *Appl. Phys. Lett.* **2008**, *92*, 171113.
[31] V. Scardaci, Z. P. Sun, F. Wang, A. G. Rozhin, T. Hasan, F. Hennrich, I. H. White, W. I. Milne, A. C. Ferrari, *Adv. Mater.* **2008**, *20*, 4040.
[32] F. Wang, A. G. Rozhin, V. Scardaci, Z. Sun, F. Hennrich, I. H. White, W. I. Milne, A. C. Ferrari, *Nat. Nanotech.* **2008**, *3*, 738.
[33] Z. M. Huang, Y. Z. Zhang, M. Kotaki, S. Ramakrishna, *Compos. Sci. Technol.* **2003**, *63*, 2223.
[34] D. Li, Y. N. Xia, *Adv. Mater.* **2004**, *16*, 1151.
[35] A. Greiner, J. H. Wendorff, *Angew. Chem. Int. Ed.* **2007**, *46*, 5670.
[36] W. E. Teo, S. Ramakrishna, *Nanotechnology* **2006**, *17*, R89.
[37] A. P. Davey, A. Drury, S. Maier, H. J. Byrne, W. J. Blau, *Synth. Met.* **1999**, *103*, 2478.
[38] H. Wolfgang, P. Alfons, G. Sung-Huan, B. Andreas, D. C. B. Donal, *Adv. Mater.* **1996**, *8*, 974.
[39] M. in het Panhuis, A. Maiti, A. B. Dalton, A. van den Noort, J. N. Coleman, B. McCarthy, W. J. Blau, *J. Phys. Chem. B* **2002**, *107*, 478.
[40] W. T. Wondmagegn, S. A. Curran, *Thin Solid Films* **2006**, *515*, 2393.
[41] J. W. Kim, N. Kotagiri, J. H. Kim, R. Deaton, *Appl. Phys. Lett.* **2006**, *88*.
[42] P. K. Ang, S. Wang, Q. Bao, J. T. L. Thong, K. P. Loh, *ACS Nano* **2009**, *3*, 3587.
[43] Y. Zhou, Q. L. Bao, L. A. L. Tang, Y. L. Zhong, K. P. Loh, *Chem. Mater.* **2009**, *21*, 2950.
[44] Y. X. Xu, H. Bai, G. W. Lu, C. Li, G. Q. Shi, *J. Am. Chem. Soc.* **2008**, *130*, 5856.
[45] Y. Si, E. T. Samulski, *Nano Lett.* **2008**, *8*, 1679.
[46] S. Stankovich, R. D. Piner, S. T. Nguyen, R. S. Ruoff, *Carbon* **2006**, *44*, 3342.
[47] P. Damlin, C. Kvarnstrom, A. Ivaska, *Electrochim. Acta* **1999**, *44*, 1919.
[48] B. Winkler, L. Dai, A. W. H. Mau, *Chem. Mater.* **1999**, *11*, 704.
[49] J. Yang, F. Y. Pang, R. Y. Zhang, Y. Xu, P. A. He, Y. Z. Fang, *Electroanalysis* **2008**, *20*, 2134.
[50] J. Jeong, S. H. Lee, N. W. Song, C. S. Lee, B. H. Chung, *Carbon* **2009**, *47*, 2124.
[51] J. L. Shui, J. C. M. Li, *Nano Lett.* **2009**, *9*, 1307.
[52] J. J. Mack, L. M. Viculis, A. Ali, R. Luoh, G. L. Yang, H. T. Hahn, F. K. Ko, R. B. Kaner, *Adv. Mater.* **2005**, *17*, 77.
[53] F. Ko, Y. Gogotsi, A. Ali, N. Naguib, H. H. Ye, G. L. Yang, C. Li, P. Willis, *Adv. Mater.* **2003**, *15*, 1161.
[54] Z. M. Huang, Y. Z. Zhang, S. Ramakrishna, C. T. Lim, *Polymer* **2004**, *45*, 5361.
[55] C. M. Roland, R. Casalini, *Macromolecules* **2003**, *36*, 1361.
[56] J. Shawn, I. J. Karl, K. Satish, *J. Polym. Sci, Part B: Polym. Phys.* **2000**, *38*, 3053.
[57] N. Dharmaraj, H. C. Park, C. H. Kim, P. Viswanathamurthi, H. Y. Kim, *Mater. Res. Bull.* **2006**, *41*, 612.
[58] N. Sonobe, T. Kyotani, A. Tomita, *Carbon* **1990**, *28*, 483.
[59] H. Kaczmarek, A. Podgorski, *Polym. Degrad. Stab.* **2007**, *92*, 939.
[60] E. Garmire, *IEEE J. Sel. Top. Quantum Electron.* **2000**, *6*, 1094.
[61] U. Keller, K. J. Weingarten, F. X. Kartner, D. Kopf, B. Braun, I. D. Jung, R. Fluck, C. Honninger, N. Matuschek, J. A. der Au, *IEEE J. Sel. Top. Quantum Electron.* **1996**, *2*, 435.
[62] Y. Sakakibara, A. G. Rozhin, H. Kataura, Y. Achiba, M. Tokumoto, *Jpn. J. Appl. Phys., Part 1* **2005**, *44*, 1621.
[63] U. Keller, *Nature* **2003**, *424*, 831.
[64] F. X. Kartner, I. D. Jung, U. Keller, *IEEE J. Sel. Top. Quantum Electron.* **1996**, *2*, 540.
[65] V. Scardaci, A. G. Rozhin, P. H. Tan, F. Wang, I. H. White, W. I. Milne, A. C. Ferrari, *Phys. Stat. Sol. B* **2007**, *244*, 4303.
[66] F. Wang, A. G. Rozhin, Z. Sun, V. Scardaci, I. H. White, A. C. Ferrari, *Phys. Status Solidi B* **2008**, *245*, 2319.
[67] H. Zhang, D. Y. Tang, X. Wu, L. M. Zhao, *Opt. Express* **2009**, *17*, 12692.